Electrochemical properties of asymmetric supercapacitor based on optimized carbon-based nickel-cobalt-manganese ternary hydroxide and sulphur-doped carbonized iron-polyaniline electrodes

Kabir O. Oyedotun, Tshifhiwa M. Masikhwa, Abdulmajid A. Mirghni, Bridget K. Mutuma, and Ncholu Manyala*.

Department of Physics, Institute of Applied Materials, SARChI Chair in Carbon Technology and Materials, University of Pretoria, Pretoria 0028, South Africa.

*Corresponding author's email: ncholu.manyala@up.ac.za, Tel.: + (27)12 420 3549.

ABSTRACT

This study describes a modified low temperature gel-method for production of low cost mixed-metal hydroxides/carbon composites electrode materials via a simple and cost-effective stirring technique. A ternary metal hydroxide of nickel, cobalt, and manganese (NiCoMn-TH) combined with activated expanded graphite (AEG) as composite electrode material (NiCoMn-TH/AEG) provided a maximum specific capacity of 116.81 mAh g^{-1} at a specific current of 0.5 A g^{-1}, measured in a three-electrode configuration in 1 M KOH aqueous electrolyte. Electrochemical measurements of the NiCoMn-TH/AEG composite material and a sulphur-doped carbonized iron PANI (CFP-S) negative electrode assembled as an asymmetric supercapacitor (SC), delivered a high energy density of 23.5 Wh kg^{-1} corresponding to a power density of 427 W kg^{-1} at 0.5 A g^{-1}. Interestingly, the assembled asymmetric *SC*, NiCoMn-TH/AEG//CFP-S gained about 68.4% of its initial specific capacitance corresponding to an energy density of ~ 31.8 Wh kg^{-1} resulting in a power density of 530.1 W kg^{-1} over a floating test of 120 h at a specific current of 1 A g^{-1}. These excellent results suggest that this composite material possesses satisfactory potential for high efficient electrode for supercapacitor applications.

KEYWORDS: Activated expanded graphite (AEG); floating test; sulphur-doped carbonized iron PANI (CFP-S); electrochemical properties; energy density.

GRAPHICAL ABSTRACT

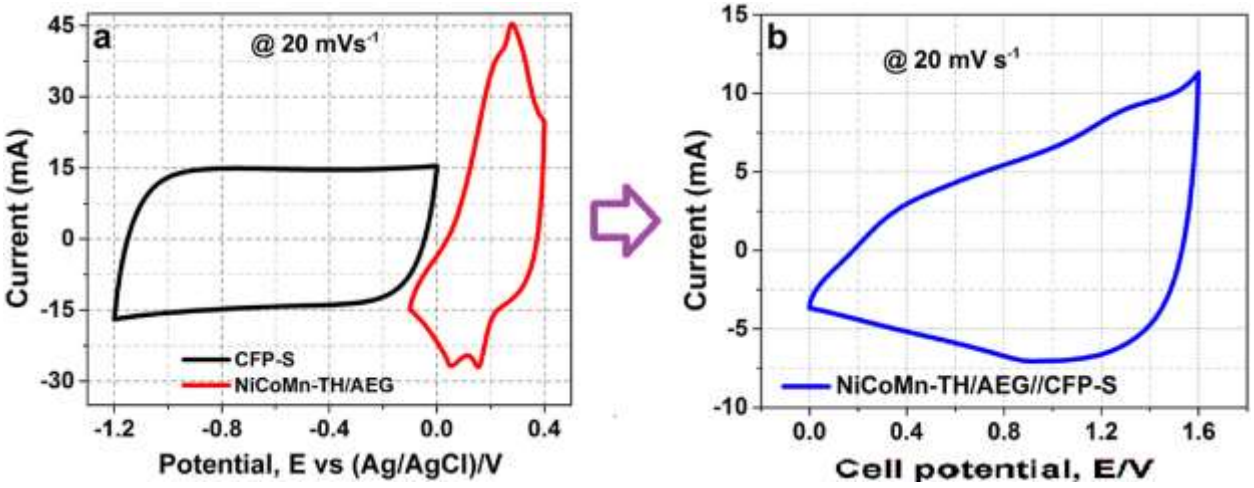

1. INTRODUCTION

The increasingly degenerating environment due to pollution coupled with the shortage of fossil fuels has become a global menace for mankind as a result of global economy rapid developments. Consequently, modern researches into developing more efficient green power sources need to be given more attention so as to totally replace the traditional fossil fuels [1–3]. Wind, solar as well as tidal energy are good alternatives owing to their replenishability and low level of pollution but are nevertheless restricted by their intermittency and poor storage performance [4]. Electrochemical energy storage devices such as supercapacitors and batteries provide a practical approach to storing electric energy through these sources [5–7].

In recent times, researchers have strived to find answers to energy storage problems such as batteries and capacitors, which are able to match with the current rate of electronic component evolution. Regrettably, we have found ourselves in the situation that a huge amount of energy can be stored in particular types of devices such as batteries, but those devices are too big, heavy,

and charge and release the stored energy somewhat slowly. Supercapacitors, an alternative device to batteries, can be charged and release energy very quickly, but hold far much less energy compared to a battery.

Supercapacitors operate electrostatically, rather than batteries that operate based on reversible chemical reactions. Theoretically, supercapacitors are charged and discharged in a number of times. The little or negligible internal resistance they possess allows them store and discharge energy with no much energy usage, and can operate at an efficiency near a hundred percent.

A supercapacitor is a high power capability electrochemical capacitor having values of capacitance far higher compared to the traditional capacitors. It bridges the gap between rechargeable batteries and electrolytic capacitors. They are typically able to store ten to a hundred times more energy per unit volume per mass compared to their electrolytic counterpart. They receive and release charge far quicker, and can endure a larger number of charge and discharge cycles than the rechargeable batteries. For a given charge, supercapacitors are nevertheless, far bigger than conventional batteries [8].

Supercapacitors are adopted in various applications. These include applications demanding swift charge-discharge cycles rather than long-term compact energy storage such as in cars, elevators, cranes, buses, and trains, in which they are employed for regenerative braking system, short-term energy storage and/or burst-mode power delivery [8-9].

Supercapacitors' properties arise through the interactions of internal materials with which they were made. Mostly, the nature of electrolytes and electrode materials' combination dictate their functionality, thermal and electrical characteristics. Numerous advantages have made supercapacitors to be applicable in consumer electronics, stationary applications to

electric/hybrid electric vehicles [9]. The various electrode materials used in supercapacitors range from metal oxides, metal chalcogenides, metal hydroxides, polymers and carbon-based materials [10]. These individual elements exhibit limited electrochemical performance due to their intrinsic material properties. To improve their supercapacitive performance, various researchers have put considerable efforts on the generation of composite nanomaterials comprising of two or more of the individual elements [11]. Thus, the resulting composite possesses synergistic properties of both elements and this can yield better electrochemical performance. To be specific, metal oxide/carbon composites have shown great potential in high-performance supercapacitors [11–13].

Since metal oxides/hydroxides suffer poor conductivities, the presence of carbon in composite of the materials serves a role of improving their electrical conductivity as well as the cycle stability and hence, impacting on their supercapacitive performance. Therefore, a combination of novel nanoscale materials properties to realize improved energy capability of supercapacitor is urgently required. In order to achieve this goal, a hybrid supercapacitor that utilizes one electrode (such as the NiCoMn-TH) that has high ion kinetics and activated carbon (such as the AEG) as the other which has got high contact area with electrolytes is required. A hybrid supercapacitor integrates the behaviours/features of a traditional supercapacitor with those of rechargeable battery and is thus, capable of enhanced electrochemical performance.

Herein, we recount the synthesis, characterization and electrochemical investigations of as-synthesized NiCoMn-ternary hydroxide (NiCoMn-TH) and its composites of activated carbon (NiCoMn-TH/AC), activated expanded graphite (NiCoMn-TH/AEG), graphene foam (NiCoMn-TH/GF), and graphene oxide (NiCoMn-TH/GO) materials via simple and cost-effective low temperature stirring technique. The AEG used in this study was selected based on its unique

interconnected sheet-like morphology cum high specific surface area (457 m^2 g^{-1}) [4]. The NiCoMn-TH/AEG composite electrode material showed enhanced electrochemical performance compared to the NiCoMn-TH material. It also displayed a maximum specific capacity of 116.81 mAh g^{-1} compared to the other materials, at a specific current of 0.5 A g^{-1} measured in a three-electrode set-up utilizing 1 M KOH aqueous electrolyte. An assembled asymmetric NiCoMn-TH/AEG//CFP-S supercapacitor demonstrated a satisfying energy density of 23.5 Wh kg^{-1} giving rise to a power density of 427 W kg^{-1} in 1 M KOH aqueous electrolyte at 0.5 A g^{-1}, alongside an excellent stability over 10000 cycles at 6 A g^{-1}. The device displays an outstanding improvement over a floating test of about 120 h. This excellent performance is ascribed to the AEG nanosheets material's unique porous and interconnected morphology that is able to ease a speedy charge diffusion mechanism.

2. EXPERIMENTAL DETAILS

2.1. Preparation of AC, GF, GO, AEG and NiCoMn-TH nanomaterials

A polymer-derived activated carbon used in this study was synthesized by dissolving a mass of GO (200 mg) in 50 mL of a mixture of polyvinyl acetate (PVA) and deionized water (DI). The resulting solution was stirred for about 15 min and then poured into a Teflon-lined autoclave for a hydrothermal process at 180 ˚C for 14 h. The resulting sample was washed and dried, and subsequently, 1 g of the sample muddled with KOH pellets (2 g) and activated at 700 ˚C for 2 h in a mixture of argon and nitrogen gases. The recovered activated carbon (AC) was washed and dried overnight in an electric oven.

The graphene foam (GF) adopted in this study was prepared via the employment of an atmospheric pressure chemical vapor deposition (APCVD) technique. A 3D-scaffold template of polycrystalline nickel (Ni) foam which was set in an APCVD quartz tube. The Ni foam was first annealed at a temperature of 1000 ˚C using both argon (Ar) and hydrogen (H_2) gasses at 300:200

sccm for 1 h to remove dissolved contaminants from the material. Thereafter, methane (CH_4) gas employed as the carbon source was flown through the reaction tube at the same temperature for 15 min, with flow rates of the three gasses being kept at 300:200:10 sccm for Ar, H_2, and CH_4, respectively. After the process, the resulting material was allowed to cool down naturally whilst adjusting the reaction tube to a cooler end of the device to facilitate even carbon deposition on the Ni foam. The recovered sample was then soaked in 120 mL of 3.5 M HCl aqueous solution and heated up to 80 ˚C to completely etch the Ni supporting structure. Thereafter, the resulting Ni foam template graphene foam was washed until neutral using deionized (DI) water and then dried at 70 ˚C overnight in an electric oven.

The gel-like reduced graphene oxide (GO) used for the synthesis of the NiCoMn-TH/GO composite was produced by adopting a modified Hummers method. Briefly, 3.0 g of $KMnO_4$ alongside a 0.5 g of graphite powder were mixed together in a beaker of concentrated H_2SO_4 (60 mL). The beaker containing the mixture stirred for 5 min and then dipped into a silicone oil-bath to maintain a uniform temperature throughout the process. Whilst stirring, 5 mL of H_2O_2 (30%) was added to the mixture with subsequently addition of 50 mL deionized (DI) water. After stirring for 3 h, the mixture was allowed to cool down naturally, re-dispersed in DI water and then sonicated for 2 h for proper reduction of the sample. The recovered sample was centrifuged and then dried overnight at 70 ˚C in an electric oven under ambient condition.

The activated expanded graphite (AEG) material used to synthesize NiCoMn-TH/AEG sample in this study was synthesized as reported in our earlier publication [14] *(more details in Supplementary information)*.

The NiCoMn-ternary hydroxide (NiCoMn-TH) composite adopted in this study, was synthesized by dissolving each of $Mn(NO_3)_2{\cdot}4H_2O$ (1.0 g), $Ni(NO_3)_2{\cdot}6H_2O$ (1.0 g) and $Co(NO_3)_2{\cdot}6H_2O$ (1.0 g) separately in DI water (50 mL). Each of the three aqueous solutions was poured into a

separate burette supported by a retort stand and then dropwise dripped simultaneously into a beaker for co-precipitation. Thereafter, 14 mL of freshly prepared 1 M NaOH was added (in drops) into the mixture whilst magnetic stirring at 40 °C. The NaOH was added to adjust the mixture's pH and influence a chemical reaction. The process was kept for a dwell time of approximately 3 h and allowed to cool down to obtain the final gel-like precipitate. After decantation, the recovered precipitate was washed two times with a 50/50 DI water/ethanol mixture (to remove dissolved metallic impurities), centrifuged twice to remove any unreacted reactants, and then transferred into an electric oven to dry overnight at 60 °C.

2.2. Synthesis of NiCoMn-ternary hydroxide/carbon-based materials composites

An optimized mass (33.5 mg) of each of AC, AEG, GF and GO was dissolved separately in a beaker of 100 mL of DI water, and then sonicated until homogeneous. Each of aqueous solutions of $Mn(NO_3)_2{\cdot}4H_2O$, $Ni(NO_3)_2{\cdot}6H_2O$ and $Co(NO_3)_2{\cdot}6H_2O$ salts prepared by dissolving 1 g each in 50 mL of DI water as mentioned in section 2.1, was poured into a separate burette mounted on a retort stand. The separate burette-containing solutions were then dripped together into a beaker containing the homogenized solution of each of the AC, AEG, GF and GO carbon materials for co-precipitation, respectively. Afterwards, 1 M NaOH (14 mL) was added in drops, and stirred at 40 °C for 3 h. The recovered mixture was left standing overnight to settle down completely, and later centrifuged and washed with deionised water and ethanol until it became neutral to litmus. The recovered solid NiCoMn-TH/AC, NiCoMn-TH/AEG, NiCoMn-TH/GF and NiCoMn-TH/GO precipitates were collected separately and dried in an oven at 60 °C for 12 h.

2.3. Synthesis of sulphur-doped carbonized iron-PANI (CFP-S) negative electrode material

The CFP-S material adopted in assembling the asymmetric NiCoMn-TH/AEG//CFP-S hybrid supercapacitor in this work was synthesized by dissolving iron (III) nitrate nonahydrate salt (0.16

g) and sulphur powder (0.04 g) in absolute ethanol (50 mL) and stirred for 5 min for uniformity. The sulphur powder was added to improve the material's pseudocapacitive property. Thereafter, 0.0125 g of as-prepared polyaniline (PANI) (*See supplementary information for synthesis of PANI*), 0.026 g carbon acetylene black (CB) together with 0.026 g PVDF were subsequently added to the solution and then stirred for 2 min. The resulting mixture was sonicated until homogeneous slurry was achieved. The mass of material precursors were cautiously chosen to have an estimate weight ratio in the order of 8:1:1 for iron (III) nitrate salt/sulphur powder/PANI, binding material (PVDF) and CB, respectively. The obtained fine slurry was pasted on a disc-like nickel foam and then transferred into an atmospheric chemical vapour deposition (APCVD) system for annealing at 850 °C for 2 h in N_2 gas flow to enable iron cations adsorbed onto the Ni foam supported sulphur-doped PANI material (CFP-S).

2.4. Characterization of as-synthesized composite materials

A Zeiss Ultra Plus 55 field emission scanning electron microscope (FE-SEM) at an operational potential of 1.0 KV was employed to acquire the materials' SEM micrographs. An EDX device attached JEOL-2100F high-resolution transmission electron microscope (TEM FEI Tecnai-F30) alongside a 200 KV acceleration voltage, was employed to analyze the elemental compositions of the CFP-S material. The materials' structural analysis (was achieved by adopting an XPERT-PRO X-ray diffractometer (XRD) (PANalytical BV, Netherlands) having reflection geometry at 2θ values (10–90°) alongside a step size of 0.01° and operating with a Cu $K\alpha$ radiation source (λ = 0.15418 nm) at 30 mA and 50 kV, respectively . A WITec alpha 300 RAS+ Confocal micro-Raman microscope (Focus Innovations, Germany) with the laser wavelength set at 532 nm was used to characterize the as-synthesized sample over a 150 s spectral acquisition time and laser power of 3 mW on the sample to avoid sample heating. A thermogravimetric analyzer, DSC-

TGA SDT Q600 V20.9 Build 20 operated at temperatures between 20 °C and 1000 °C in air at a ramping rate of 10 °C/min was employed to analyze the thermal stability of the samples.

2.5. Electrochemical characterization

The electrodes utilized in this research were fabricated by mixing 80 wt% of the active material, with 10 wt% conductive acetylene black as a conducting agent alongside 10 wt% of PVDF binder. The mixture was muddled together by adding some drops of N-methyl-2-pyrrolidone (NMP) solvent and stirred uniformly to make slurry. The formed slurry was applied pasted onto nickel foam (1 cm x 1 cm) adopted as current collector, and then dried overnight at 60 °C. Electrochemicalperformance of the fabricated electrodes was examined by employing a Bio-Logic VMP300 potentiostat (Knoxville TN 37,930, USA) guilded by the EC-Lab® V1.40 software via a three-electrode system of measurement. The electrochemical investigations were done by adopting a glassy carbon as the counter electrode, Ag/AgCl as the reference electrode, and the as-synthesized materials as the working electrodes. In this study, all investigations were done by utilizing 1 M KOH electrolyte at 25 ˚C. The active materials' mass loading was determined to be ca. 2.54, 2.54, 2.56, 2.55, and 2.61 mg for pristine NiCoMn-TH, NiCoMn-TH/AC, NiCoMn-TH/AEG, NiCoMn-TH/GF and NiCoMn-TH/GO composite electrodes, respectively. The as-prepared samples cyclic voltammetry (CV) tests were run at various scan rates ranging from 1 to 50 mV s^{-1} in an operating potential ranging from -0.1 V to 0.4 V against an Ag/AgCl reference electrode. Galvanostatic charge/discharge (GCD) measurement was performed at various specific currents ranging from 0.5 to 10 A g^{-1} in a working potential ranging from -0.1 V to 0.4 V. The samples' electrochemical impedance spectroscopy (EIS) was skilfully guided through an open-circuit potential at frequencies ranging from 10 mHz to 100 kHz.

The specific capacity, Q_s (mAh g^{-1}), and the energy efficiency as a function of mass of the single electrode materials by means of GCD profiles were determined by employing the relations stated below [15]:

$$Q_s = \frac{I_d * \Delta t}{3.6} \quad (1)$$

$$\eta_E = \frac{E_d}{E_c} \times 100 \quad (2)$$

From the above, I_d is applied specific current (A g^{-1}). Δt accounts for time (s) difference taken for a full discharge cycle while η_E, E_d and E_c represent the energy efficiency, discharge energy as well as charge energy derived by integrating the area under the charge/discharge profile, respectively.

The asymmetric device's specific capacitance, C_s, alongside its energy and power densities as a function of specific current were estimated via the slope of the discharge curve using the relations:

$$C_s = \frac{I_d \times \Delta t}{\Delta E} \quad [F\ g^{-1}] \quad (3)$$

$$E_d = 0.5\ C_s \Delta E^2 = \frac{1000 \times C_s \Delta E^2}{2 \times 3600} = \frac{C_s \Delta E^2}{7.2} \quad [Wh\ kg^{-1}] \quad (4)$$

$$P_d = 3.6 \times E_d / \Delta t \quad [kW\ kg^{-1}] \quad (5)$$

C_s is electrode's specific capacitance calculated with respect to active material's effective mass. I_d is applied specific current (A g^{-1}). $\Delta E\ (= E_o - E_{IR-drop})$ is the change in operating potential or cell potential (V), Δt is time (s) discharged by the electrode, while E_d and P_d represent the energy and power densities, respectively.

The asymmetric *SC's* coulombic efficiency, C_E was determined over a cell potential, E (V) via the equation:

$$C_E = \frac{C_{sd}}{C_{sc}} \times 100\% \quad (6)$$

where C_{sc} and C_{sd} denote the specific capacitance for charge and discharge processes, respectively.

The prepared asymmetry *SC* could operate in a larger potential window, *ca.* 1.60 V. The effective mass on each electrode was proportionately derived via the charge balance equation, $Q_+ = Q_-$ to ensure optimal performance of the *SC,* while the stored charge on respective electrode can be expressed as [16]:

$$Q = Q_s \times m\,\Delta E \quad (7)$$

From equation (7), Q (C) is charge being stored on respective electrode, Q_S (mAh g^{-1}) represents specific capacity of a single electrode in line with effective active material's mass , while m (g) denotes active material's effective mass and ΔE (V) is operating potential of the electrode.

Furthermore, the balancing of masses between the electrodes of the *SC* was precisely figured out by adopting equation (8) as stated below [17]:

$$\frac{m_+}{m_-} = \frac{Q_{s-}\ \Delta E_-}{Q_{s+}\ \Delta E_+} \quad (8)$$

3. RESULTS AND DISCUSSION

3.1. Physical characteristics of the materials

Fig. 1 is a demonstration of SEM morphology for all as-synthesized composite samples. Fig. 1 (a) represents a high magnification SEM image of NiCoMn-TH sample, showing a stacked flake-like structure, while in Fig. 1 (b) it can be observed that NiCoMn-TH/GO is made up of agglomerated sheet-like particles. This is as a result of the addition of GO in the composite. Fig. 1 (c) shows the SEM image of NiCoMn/AEG at high magnifications. The AEG sheet-like

structure can be seen to be evenly covered by the NiCoMn-TH nanoflakes. Fig. 1(d-e) show agglomerated flake-like morphology of the NiCoMn-TH/AC and NiCoMn-TH/GF materials. Fig. S1 *(See supplementary information)* shows the SEM images of (a) an activated carbon, (b) a graphene foam, (c) an AEG and (d) a GO material adopted in the synthesis of the NiCoMn-TH/AC, NiCoMn-TH/GF, and NiCoMn-TH/AEG and NiCoMn-TH/GO composite materials, respectively. The figure depicts a porous morphology for the AC (Fig. S1 (a)), and sheet-like morphologies for both GF (Fig. S1 (b)) and AEG (Fig. S1 (c)) materials, respectively, while a gel-like morphology was observed for the GO material. The observed morphology is typical for the adopted materials, respectively. Fig. S2 (a) shows a SEM image of CFP-S material used for fabrication of NiCoMn-TH/AEG//CFP-S asymmetric device. The material can be noticed to be composed of mainly agglomerated nano-sized grain particles.

The EDX analysis in Fig. S2 (b) reveals presence of carbon (52.3 wt. %), iron (31.4 wt. %), and sulphur (11.9 wt. %) as main elements present in the material. The presence of Cu, Co, Cr, Tb and Hf as trace elements is attributed to the grid sample holder adopted for the EDX measurement.

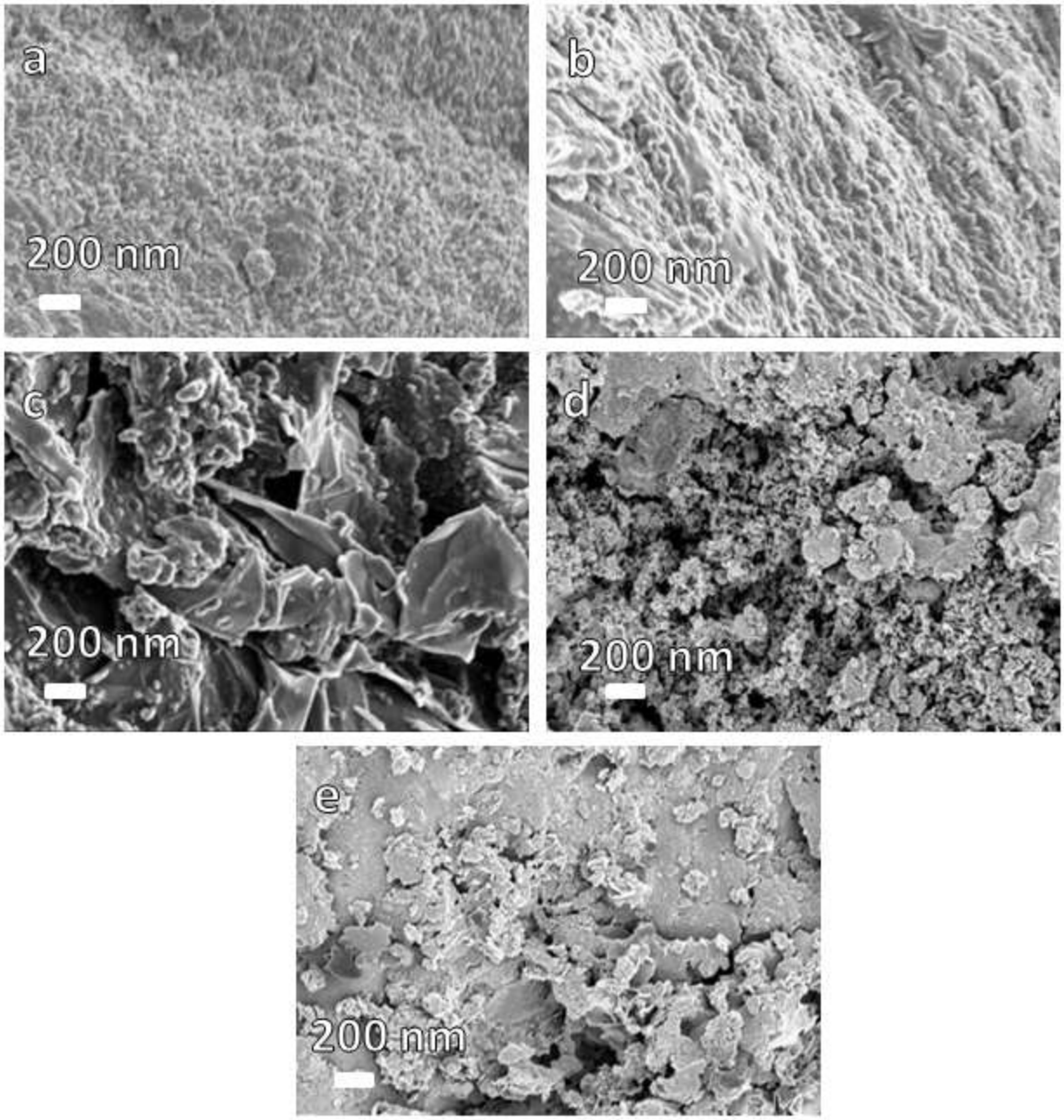

Fig. 1. SEM images of the as-prepared (a) NiCoMn-TH, (b) NiCoMn-TH/GO, (c) NiCoMn-TH/AEG, (d) NiCoMn-TH/AC, and (e) NiCoMn-TH/GF at high magnifications, respectively.

Fig. 2 (a) shows a representative powder XRD pattern of all the as-synthesized composite materials. The XRD reveals a characteristic diffraction pattern of the phases of transition metal hydroxide, which agrees strongly with patterns of $Ni(OH)_2$, $Co(OH)_2$ as reported in our earlier work [18], and $Mn(OH)_2$, with ICSD card nos. 28101, 88940, and JCPDS no. 73-1604

standards, respectively. The observed peak at nearly 2θ = 27°, corresponding to the (002) plane of graphitic carbon indicates the inclusion of carbon material in the composites. Every peak in the composite material reveals the presence of NiCoMn-TH in composite with carbon materials. Fig. S2 (c) *(see supplementary information)* reveals the result of X-ray diffraction (XRD) employed to investigate the structure of CFP-S negative electrode material used in fabricating the asymmetric NiCoMn-TH//CFP-S device. The XRD spectra measured in an angular range of 5 to 90 illustrate the appearance of peaks at angular positions 2θ equals 21.74, 34.78, 39.33, 44.0, 50.71, 52.35, 57.66, 62.45, 66.13, 74.98, 84.5° corresponding to reflection planes 002, 010, 002 (011), 012, 031, 012, 320, 301, 110, 013, 401 and 002 indexed in line with an ideal matching Inorganic Crystal Structure Database (ICSD) card numbers: 16593 for Fe_3C, 98-016-8077 for FeS (Pyrrhotite and Troilite), and 42-1340 for FeS_2, respectively. Besides, the spectra indicate the presence of Fe_3C in reference to Joint Committee on Powder Diffraction Standards, JCPDS no. 06-0686; Standard carbide diffraction curve PDF-2 Data base-2, showing a sharp peak for graphitic carbon; $2\theta = \sim 40°$ (002) reflection.

Fig. 2 (b) displays the Raman spectrum of all the composites. The Raman spectrum shows modes at 121, 176, 518 and 625 cm^{-1} which were compared to those reported in the literature [18,19] for $Ni(OH)_2$, $Co(OH)_2$, and $NiCoMnO_2$. The peak observed around 121 cm^{-1} is owing to the radial breathing mode (RBM, 100–300 cm^{-1}) of carbon in the composite [20]. The active mode at about 176 cm^{-1} is a characteristic feature of typical MnO_2 phase as well as the material's restricted translation mode of the hydrogen-bonded water molecules [21,22]. The 518 cm^{-1} mode noticed for all the composite materials is due to the material's lattice vibration [23,24]. Also, the samples showed active mode at 625 cm^{-1} wavenumber which is in agreement with significant vibrational attributes of MnO_2 reported earlier at about 500, 585, and 625 cm^{-1} on some other closely related materials [25,26], hinting the presence of Mn-O compound in the composite

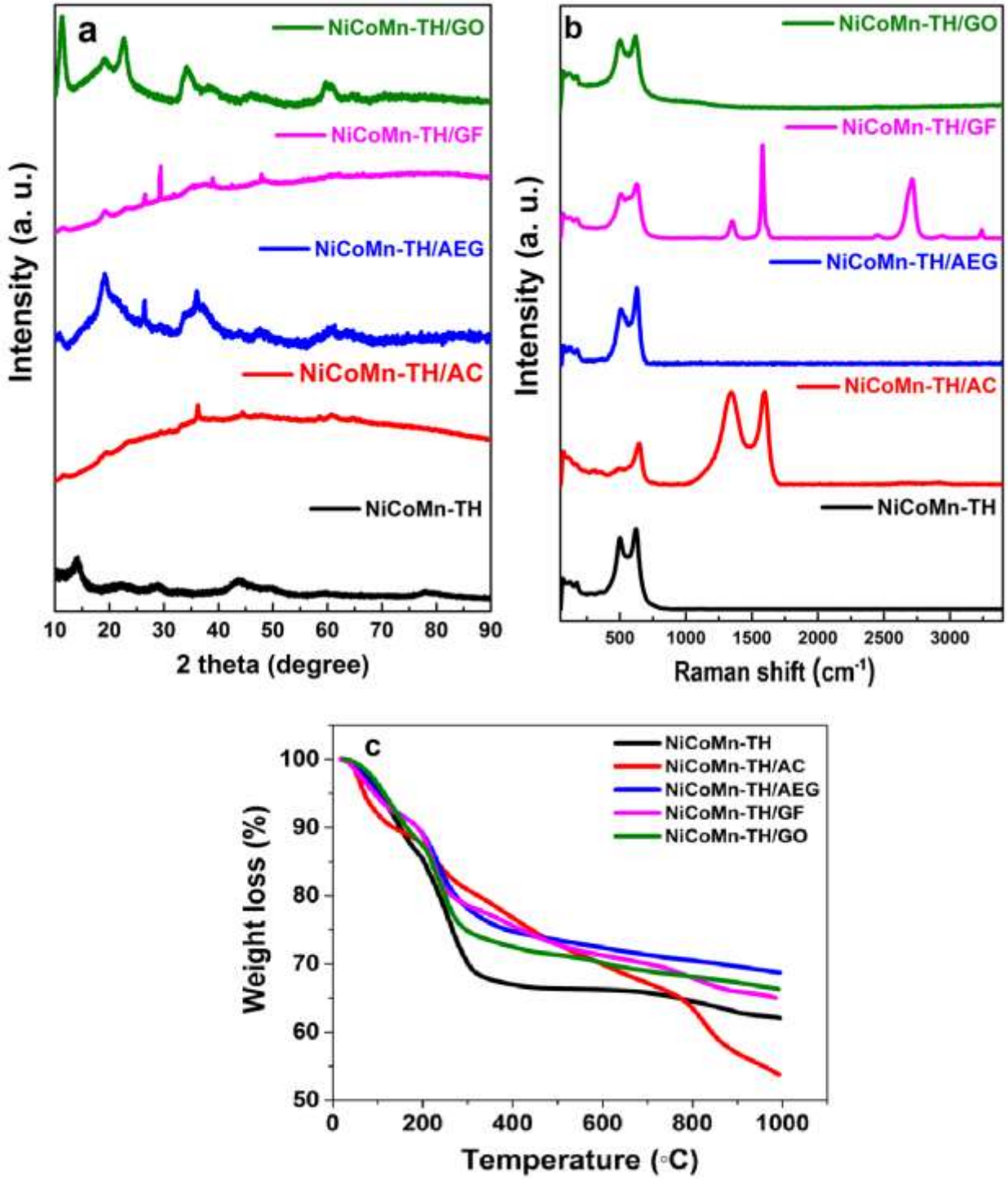

Fig. 2. (a) XRD patterns, (b) Raman spectra, and (c) TGA curves of as-prepared nanocomposite materials.

material. The NiCoMn-TH/GO was noticed to display a similar Raman spectrum except for a shift of peaks at around 505 and 617 cm^{-1} which could be ascribed to the inclusion of oxygen in the material. The D and G bands observed the NiCoMn-TH/AC composite at ~1350 cm^{-1} and ~1604 cm^{-1} suggest a disordered carbon owing to the breathing modes of sp^2 rings activated through a dual resonance effect in the presence of defects as well as the phonon in-plane stretching mode of the C−C bond in the graphitic materials [27], respectively. Fig. 2 (c) depicts the TGA curves for all the NiCoMn/carbon materials.

From the TGA profiles in Fig. 2(c), a slight weight loss at about 157 °C was noticed for the NiCoMn/AEG material, which is attributed to loss of interfacial-adsorbed moisture in the material. The weight loss at nearly 300 °C is an indication of evaporation of adsorbed water molecules [28,29]. Further weight loss is as a result of further heating on the samples [30]. Based on the residual weight of the material; 68.76 % at about 991 °C, the amount of AEG sample contained in the composite material was calculated to be roughly 31.24 wt%. A residual weight of nearly 66.31 %, 64.81 % and 53.88 % at around 990 °C was observed for the NiCoMn/GO, NiCoMn/GF and NiCoMn/AC materials, respectively. The amount of GO, GF and AC in the respective NiCoMn/carbon materials was estimated to be about 33.69 wt%, 35.19 wt% and 46.12 wt%, respectively, higher amounts compared to that of the AEG material.

3.2. Electrochemical analysis

3.2.1. Electrochemical analysis of single electrodes

Fig. 3 (a) shows the associated CV profiles of the as-prepared electrode materials at 20 mV s^{-1} scan rate. From figure 3 (a), the CV curve of NiCoMn/AEG shows a higher current response indicating a higher specific capacity when compared to the other samples. Fig. 3 (b) displays the galvanostatic charge-discharge (GCD) curves of NiCoMn-TH, NiCoMn/AC, NiCoMn/AEG, NiCoMn/GF and NiCoMn/GO samples at various specific currents in a working potential

ranging from -0.1–0.4 V, respectively. The observed indefinite GCD curves display faradic properties of the electrode materials, with the NiCoMn/AEG showing higher discharge time compared to the other two samples. Fig. 3 (c) shows the specific capacity of a single electrode calculated according to equation 1 via a less defective charge-discharge technique profiles, and plotted against its respective as-synthesized composite material at a specific current of 0.5 A g^{-1}. From Fig. 3 (c), the NiCoMn/AEG composite is observed to exhibit a higher value of 116.81 mAh g^{-1} compared to the other composite materials. Fig. 3 (d) is a display of Nyquist impedance plots of the samples evaluated at a potential of 0.0 V and frequencies ranging from 10 mHz – 100 kHz. A small semi-circle was observed for all the samples in the high-frequency region is an indication of a resistance occurring as a result of electron transfer from the electrode to the electrolyte. It can be observed that the NiCoMn/AEG sample diffusion path length is shorter, and closer to the ideal vertical line suggesting that the material is more electrochemically conductive than NiCoMn-TH, NiCoMn/AC, NiCoMn/GF and NiCoMn/GO composite materials.

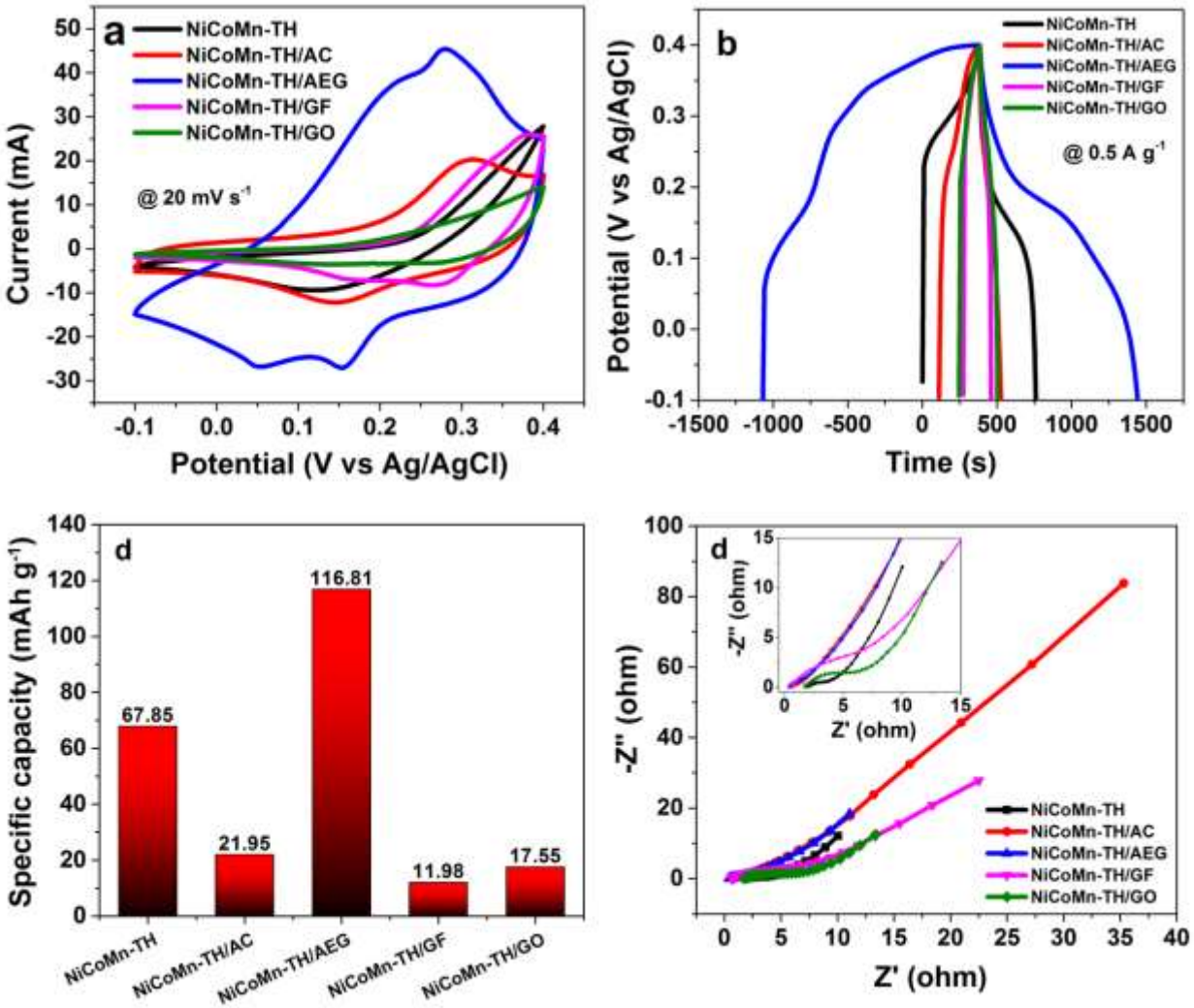

Fig. 3. (a) CV curves at a scan rate of 20 mVs^{-1}, (b) GCD curves at a specific current of 0.5 A g^{-1}, (c) specific capacity calculated for all the samples at a specific current of 0.5 A g^{-1}, and (d) Nyquist impedance plot for the samples, respectively.

Due to poor electrochemical properties of NiCoMn-TH/AC, NiCoMn-TH/GF and NiCoMn-TH/GO samples compared to both NiCoMn-TH and NiCoMn-AEG electrodes (as shown in Fig. 3), a further electrochemical comparison was done on the NiCoMn-TH/AEG electrode material because of its superior electrochemical behavior over the other samples. Fig. 4 (a) and (b) show the full CV and GCD curves of the more electrochemically stable NiCoMn/AEG at various scan rates and at various specific currents, respectively. According to equation 1, the values of

specific capacity of the NiCoMn/AEG electrode were estimated and indicated against its specific currents as depicted in Fig. 4 (c). The NiCoMn-TH/AEG composite electrode showed a maximum specific capacity of 116.81 mAh g^{-1} at a specific current of 0.5 A g^{-1}. Fig. 4 (d) depicts the specific capacity retention alongside energy efficiency for the NiCoMn/AEG electrode against the charge-discharge cycle number for over 2000 cycles. The observed high capacity retention of 76.4% and high energy efficiency (94.5%) estimated from equation 2, can be attributed to a higher electronic conductivity owing to its low equivalent series resistance, R_S value (0.118 Ω) compared to the other materials (Fig. 3 (d)).

The fitted EIS Nyquist plot of the NiCoMn/AEG is displayed in Fig. 5 (a), with its equivalent circuit as the inset, which was used for fitting the data. The circuit in the inset presents an equivalent series resistance denoted as R_1 that opposes current flow through the electrolyte wherewith the ions migrate, in connection with a charge transfer resistance (R_2), a leakage resistance (R_3), and a single resistance (R_4) proportionately. The constant phase elements designated as Q are due to a distribution of relaxation times following the inhomogeneity occurring between the electrode and electrolyte interface [27, 31].

Fig. 5 (b) shows its Nyquist impedance curves before and after a 2000-cycling test, showing a slight deviation from the initial diffusion path length. This slight deviation can be ascribed to a leakage resistance owing to the Faradaic charge transfer process [31]. The equivalent series resistance, R_1 (0.118 Ω) initially obtained for the material was observed to be constant even after the 2000 cycles test. This indicates the material's good capacitance over a long cycling test. Table S1in the supplementary information depicts a summary of evaluated values of R_1, R_2, R_3, R_4 and Q using a ZFIT program software associated with the Bio-Logic VMP300 potentiostat. Fig. 5 (c) exhibits CV profiles of the material taken before and after the test. The material

portrayed no noticeable current loss, which shows its good capacitance over the stability test. The good behavior can be assigned to the constant surface area available to react with the electrolyte when the aggregation dissolved to some degree in the electrolyte [32].

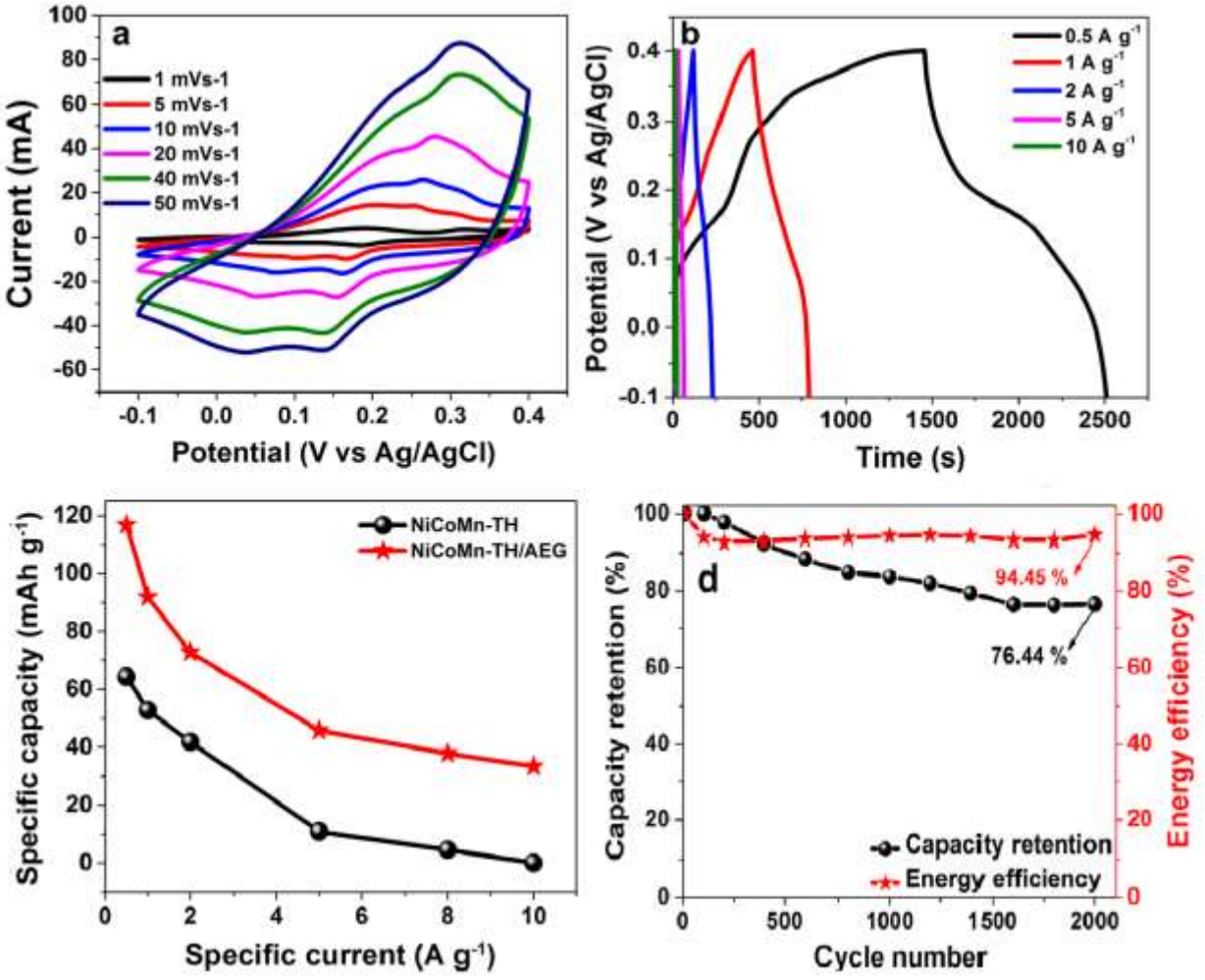

Fig. 4. (a) the CV curves of NiCoMn-TH/AEG at various scan rates, (b) GCD curves of NiCoMn-TH/AEG at different specific currents, (c) a plot of specific capacities against specific currents for NiCoMn-TH/AEG and NiCoMn-TH, and (d) distinctions of specific capacity and energy efficiency of NiCoMn-TH/AEG electrode against cycle numbers examined at 5 A g^{-1} in 1 M KOH electrolyte.

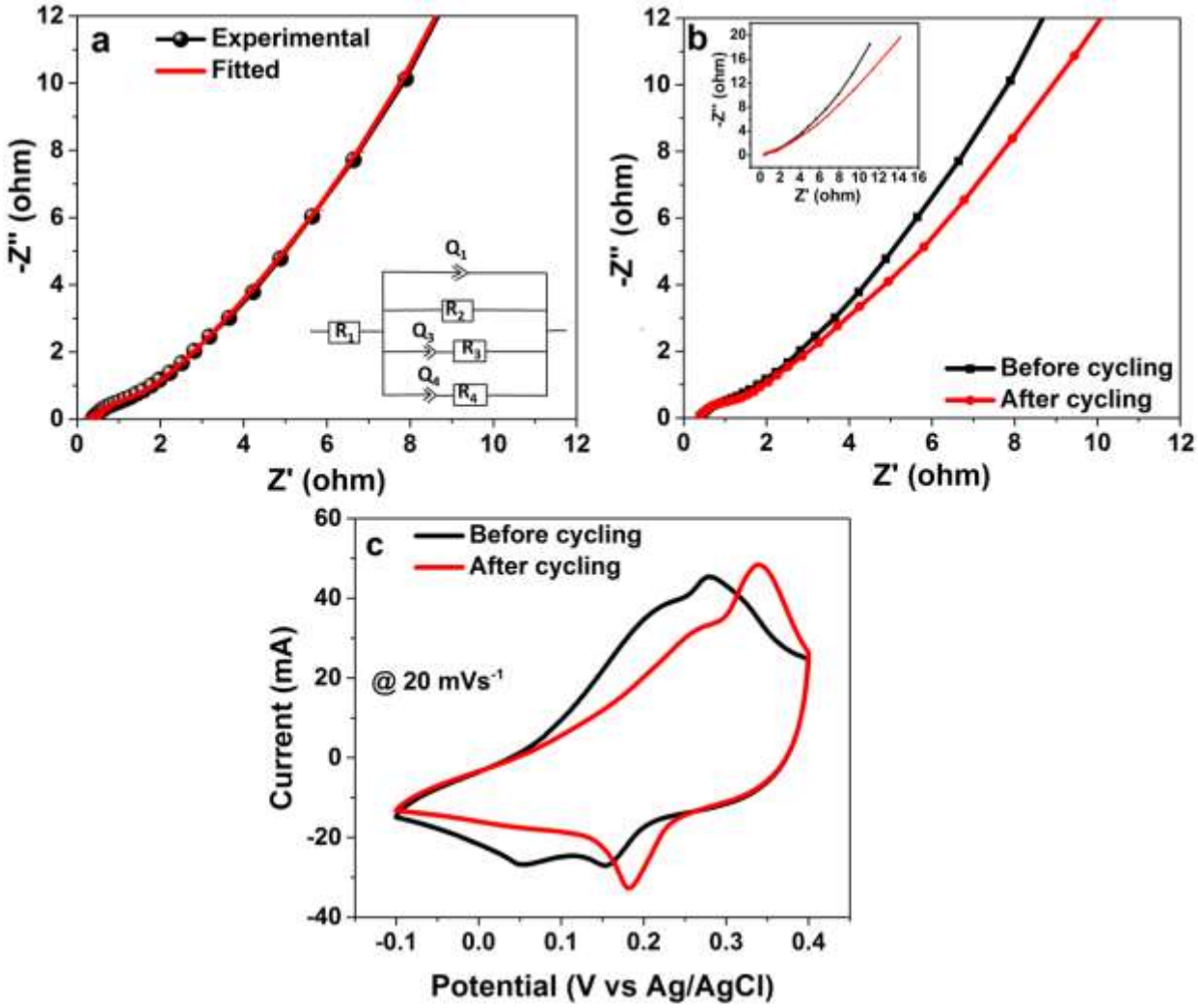

Fig. 5. (a) Fitted Nyquist plot and the equivalent circuit (inset), (b) Nyquist plot before and after 2000 charge-discharge cycles at a specific current of 5 A g^{-1}, and (c) CV curves before and after 2000 charge-discharge cycles for the NiCoMn-TH/AEG electrode.

3.2.2. Full-cell electrochemical investigations of the asymmetric NiCoMn-TH/AEG //CFP-S hybrid supercapacitor

Owing to the enhanced electrochemical properties of the NiCoMn-TH/AEG positive materials in the above preceding section (3.2.1.), an asymmetric supercapacitor, *SC* was assembled utilizing the sulphur-doped carbonized iron PANI (CFP-S) as negative electrode material, and named as NiCoMn-TH/AEG//CFP-S having effective mass balance ratio deduced in line with equation 9,

as 0.7: 1.0 resulting in an effective mass loading of ~ 2.1 and 3.0 mg cm^{-2} for both NiCoMn-TH/AEG and CFP-S, respectively. The study about detailed characterization of CFP-S negative electrode material adopted for fabrication of NiCoMn-TH/AEG//CFP-S device in this work is on-going in our research group.

The NiCoMn-TH/AEG positive working electrode prepared as stated earlier in experimental section *(see section 2.5)*. The overall area mass loading of both active electrode materials making up the asymmetric *SC* was determined as ~ 5.1 mg cm^{-2} using a digital weighing balance. The electrochemical testing of the assembled asymmetric SC was run via a two-electrode system utilizing a standard 2032 grade coin cells and a Watman Celgard paper-based separator in 1 M KOH aqueous electrolyte.

Fig. 6 (a) portrays the CV curves of the device at various scan rates. The nearly rectangular CV profiles of the device reveal no capacitance decay at various scan rates, which indicates its swift ion transport mechanism and good rate capability [33]. The considerably symmetrical CV curves reveal some contributions from the hybrid NiCoMn-TH/AEG//CFP-S device faradaic process. Fig. S3 (a and b) in the supplementary information displays the CV and CD profiles of the as-synthesized NiCoMn-TH/AEG nanocomposite and CFP-S electrodes, respectively using a three-electrode set-up. The synergistic effect from a combination of the apparently electric double-layer capacitive (EDLC) CFP-S and faradaic NiCoMn-TH/AEG electrode materials as displayed in Fig. S3 gives rise to the CV and CD profiles that are much comparable to that of an EDLC material, as shown in Fig. 6 (a and b). Fig. 6 (b) portrays the CD curves of the asymmetric NiCoMn-TH/AEG//CFP-S *SC* at distinct specific currents in a two-electrode system. The CD triangular curves of the device display ideal linear discharge behaviour, indicating its double-layer capacitive nature and good reversibility. The assembled device could work satisfactorily in

a much larger operating potential of about 1.6 V estimated based on a combined effect of the respective electrodes' operating potential limits.

The device's specific capacitances were calculated at various specific currents in line with equation 4, and plotted as shown in Fig. 6 (c). The device gave a maximum specific capacitance of about 66 F g^{-1} at 0.5 A g^{-1}, corresponding to a satisfying energy and power densities of 23.5 Wh kg^{-1} and 427 W kg^{-1}, respectively, as shown in Fig. 6 (d).

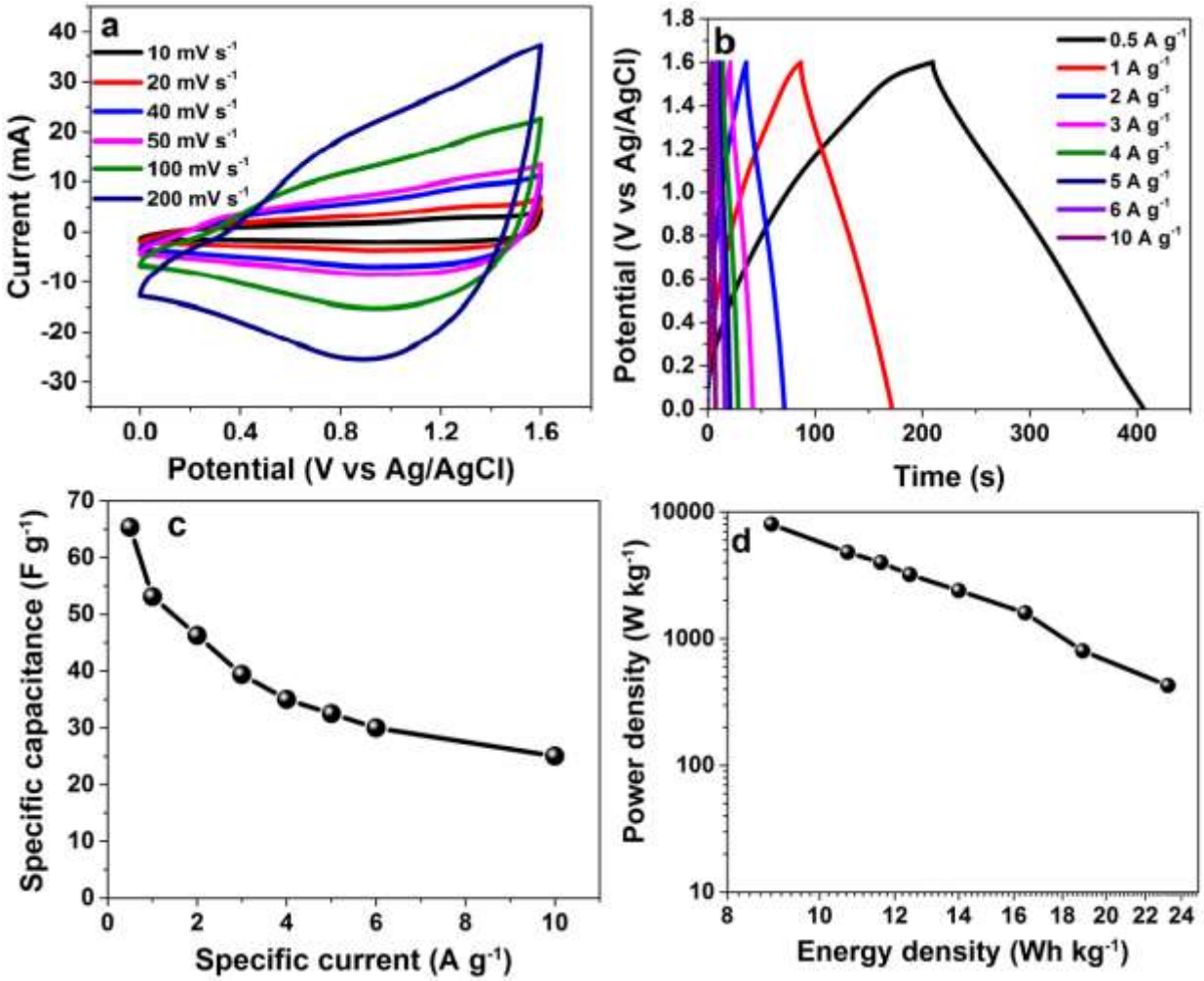

Fig. 6. (a) CV curves of NiCo-Mn-TH/AEG//CFP-S at various scan rates, (b) GCD curves of NiCo-Mn-TH/AEG//CFP-S at various specific currents, (c) specific capacitance of NiCo-Mn-TH/AEG//CFP-S evaluated at various specific currents, and (d) Ragone plots of the asymmetric SC.

The values of energy density obtained at different specific currents for the asymmetric device in this work depict considerable enhancement compared to other similar devices in the literature. Such devices include: Co_2P nanostructure//graphene; 8.8 Wh kg^{-1} at power density of 6000 W kg^{-1}, at 1 A g^{-1} [34], $Co(OH)_2$/GNS//AC/CFP; 19.3 Wh kg^{1} at power density of 187.5 W kg^{-1}, at 0.25 A g^{-1} [35], $NiCo_2O_4$ NSs@HMRAs//AC; 15.42 Wh kg^{-1} at power density of 7800 W kg^{-1}, at 5 mV s^{-1} [36], and $NiCo_2S_4$//C; 22.8 Wh kg^{-1} at power density of 160 W g^{-1}, at 1 mA cm^{-2} [37]. The results in this current study are of great interest, not only for describing a modified low temperature gel-method for production of electrode materials, but also for the development of promising enhanced *SC* electrode materials with excellent electrochemical behaviours.

Fig. 7 (a) shows a plot of both coulombic efficiency and capacitance retention for the *SC* against the cycle numbers. The device showed an excellent coulombic efficiency of nearly 100% over 10,000 CD cycles, with satisfying capacitance retention stability (87.8 %) at a specific current of 6 A g^{-1}. This is suggesting that even over a 10,000 continuous cycling test, the device does not experience significant defective structural or phase change of the electrode materials. The excellent performance is assigned to a significant porous and interconnected micrograph of the AEG material nanosheets that is able to accelerate a rapid charge transport mechanism [14]. The floating also referred to as the voltage-holding test, is an established alternative and dependable technique for analyzing the stability of supercapacitor electrodes [38]. It provides a factually correct resistance effect after being subjected to maximum potential, which may be near to practical application. Floating test proffers a direct insight into the probable effect and degradation phenomena that might take place during the electrochemical process in EDLC cells at significant potentials in comparison with the conventional cycling test that often provides no degradation [38–40]. In this work, the technique was performed at a constant load by holding the cell at its highest potential (1.6 V), and estimating the capacitance over the entire period as

depicted in Fig. 7 (b) in a repeated sequence. Fig. 7(b) displays a variation of the device's specific capacitance over a floating time of 120 h at a peak operating potential of 1.6 V, with the specific capacitance being monitored at a time interval of 10 h. Interestingly, the device delivers an improved specific capacitance of about 68.4% over its initial value, giving a specific capacitance of nearly 89.45 F g^{-1} (as shown in Fig. 7 (b)) against its initial value of 53.13 F g^{-1}, corresponding to an energy density of ~ 31.8 Wh kg^{-1}, with a power density of 530.1 W kg^{-1} over a floating test for 120 hours at 1 A g^{-1}, respectively. From the CV curves in Fig. 7 (c), it could be noticed that the device tends to recover after a long floating time of 120 h. The enhanced area observed under the CV curve after the floating test is an indication of improved specific capacitance of the device, which is attributed to more charge separation as well as improved polarity of electrode materials in the cell [41]. The improved electrochemical performance of the device over the floating test is ascribed to the accessibility of some hidden pores by the electrolyte [41]. Fig. 7 (d) shows an EIS Nyquist graph of the device adopted to investigate the diffusion kinetics on the surface of its electrodes. In the Figure, device's equivalent series resistance, R_S was estimated to be ~ 3.7, 2.6 and 1.8 Ω before cycling, after 10000 cycling and over a floating of 120 h tests, respectively, indicating a good material's recovery and enhanced conductivity of the device after being subjected to a long cycle/period stability test. The device shows no distinct semicircle in the high-frequency region over a floating test of 120 h, revealing a very low charge transfer resistance and fast mass transport between its electrodes and the electrolyte. Fig. 7 (d) shows an EIS Nyquist graph of the device adopted to investigate the diffusion kinetics on the surface of its electrodes.

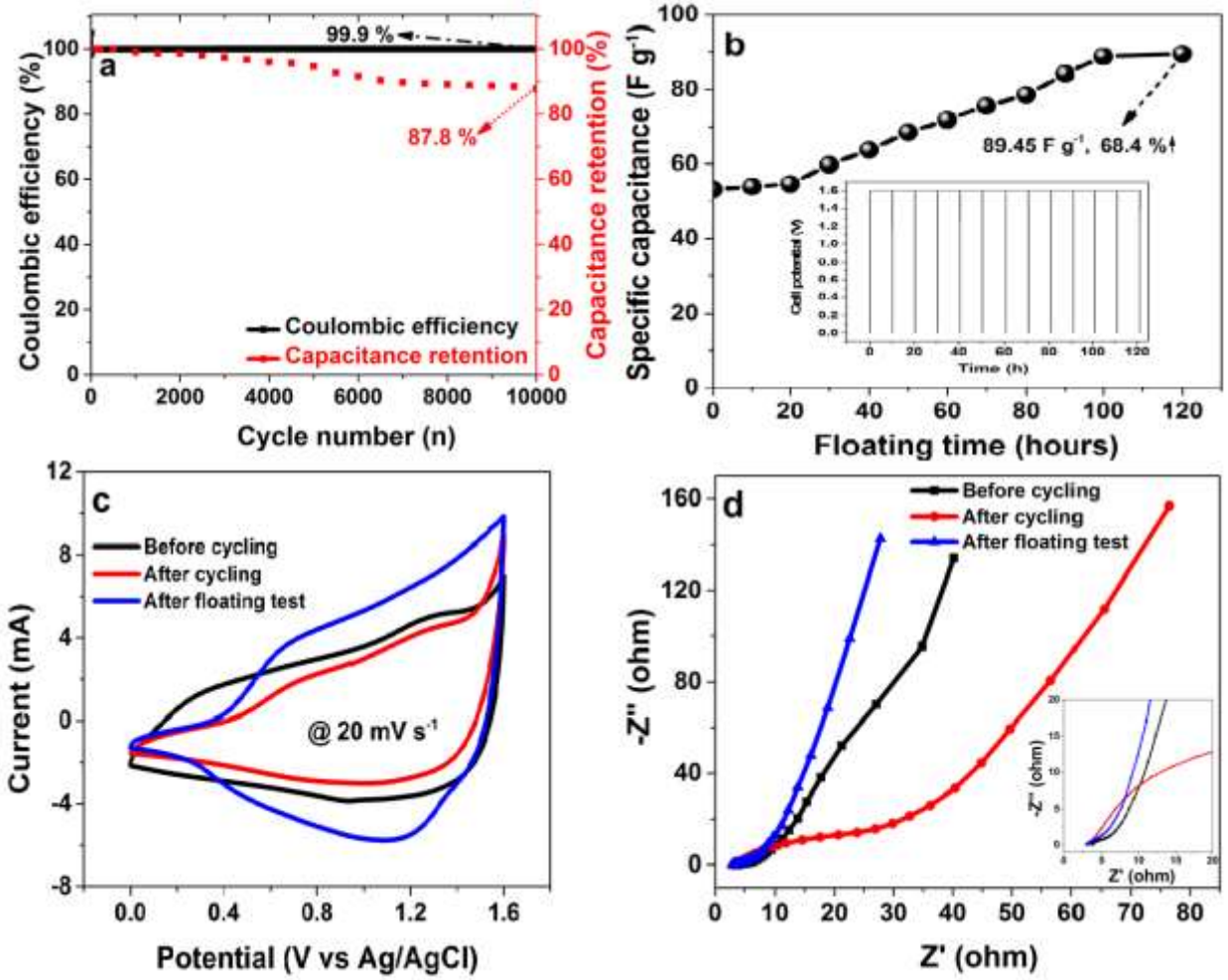

Fig. 7. (a) Cyclic performance, (b) plot of specific capacitance against potentiostatic floating time, (c) CV curves, and (d) EIS plot before cycling, after cycling and after voltage holding test for the NiCoMn-TH/AEG//CFP-S asymmetric *SC*.

Table S2 in the supplementary information displays the values of R_S and R_{CT} extrapolated from the points of intersection on the real axis of Nyquist plots of the device, and by using the "Circular Fit" software integrated with the Bio-Logic system employed in this work, respectively. In the table, a reduced value of R_{CT} was noticed for the device after the floating test, which further confirms its improved performance after the long hours of voltage holding test.

After the floating test, the diffusion path length was observed to have shifted closer to the ideal vertical line compared to the path length previously obtained for the device before cycling test of over 10000 cycles, showing the device's improved electrochemical performance. The device shows better capacitance after the floating test, compared to that before and after cycling test. This indicates the availability of sufficient active material reacting with the electrolyte during the electrochemical reaction, in spite of the long period of floating.

4. CONCLUSION

NiCoMn-ternary hydroxide (NiCoMn-TH) and its composites with graphene oxide (NiCoMn-TH/GO) as well as activated expanded graphite (NiCoMn-TH/AEG) electrode materials were synthesized through a simple and cost-effective low temperature stirring technique. The electrochemical conduct of the materials measured in a three-electrode system in 1 M KOH proved a notable enhancement on specific capacity providing a value of 116.81 mAh g^{-1} for NiCoMn-TH/AEG contrast to 21.95 mAh g^{-1}, 11.98 mAh g^{-1}, 17.14 mAh g^{-1}, and 67.85 mAh g^{-1} for NiCoMn-TH/AC, NiCoMn-TH/GF, NiCoMn-TH/GO and NiCoMn-TH at 0.5 A g^{-1}, respectively. A fabricated asymmetric NiCoMn-TH/AEG//CFP-S supercapacitor in 1 M KOH proved a satisfying energy density of 23.5 Wh kg^{-1}, providing an equivalent power density of 427 W kg^{-1} at 0.5 A g^{-1}, alongside an excellent coulombic efficiency (99.92 %) and retaining ~ 87.8 % of its initial capacitance for over 10,000 cycles at 6 A g^{-1}. The asymmetric supercapacitor displays excellent stability over a floating test for over 120 h at a specific current of 1 A g^{-1}, yielding an enhanced energy density of 31.8 Wh kg^{-1} compared to its initial value of 18.9 Wh kg^{-1}, and a corresponding power density of 530.1 W kg^{-1}, respectively, at a specific current of 1 A g^{-1}. The moderate AEG doping via a modified low temperature gel-method of production has greatly improved the electrochemical performance of the NiCoMn-TH electrode material.

ACKNOWLEDGEMENTS

This study is supported by the South African Research Chairs Initiative of the Department of Science and Technology and National Research Foundation of South Africa (Grant No. 61056). The opinion, finding, and conclusion specified herein are those of the author(s), and the NRF is not any form accountable in this regard. The authors are grateful to Dr. Farshad Barzegar of the University of Pretoria for material contribution. K. O. Oyedotun acknowledges financial support from the University of Pretoria and National Research Foundation (NRF).

REFERENCES

[1] P. Yang, P. Sun, W. Mai, Electrochromic energy storage devices, Mater. Today. 19 (2016) 394–402. doi:10.1016/j.mattod.2015.11.007.

[2] P. Gu, M. Zheng, Q. Zhao, X. Xiao, H. Xue, H. Pang, Rechargeable zinc–air batteries: a promising way to green energy, J. Mater. Chem. A. 5 (2017) 7651–7666. doi:10.1039/C7TA01693J.

[3] F. Zhang, L. Qi, Recent Progress in Self-Supported Metal Oxide Nanoarray Electrodes for Advanced Lithium-Ion Batteries, Adv. Sci. 3 (2016) 1–29. doi:10.1002/advs.201600049.

[4] W. Tang, Y. Zhu, Y. Hou, L. Liu, Y. Wu, K.P. Loh, H. Zhang, K. Zhu, Aqueous rechargeable lithium batteries as an energy storage system of superfast charging, Energy Environ. Sci. 6 (2013) 2093. doi:10.1039/c3ee24249h.

[5] B. Li, P. Gu, Y. Feng, G. Zhang, K. Huang, H. Xue, H. Pang, Ultrathin Nickel–Cobalt Phosphate 2D Nanosheets for Electrochemical Energy Storage under Aqueous/Solid-State Electrolyte, Adv. Funct. Mater. 27 (2017) 1605784. doi:10.1002/adfm.201605784.

[6] W. Zuo, R. Li, C. Zhou, Y. Li, J. Xia, J. Liu, Battery-Supercapacitor Hybrid Devices: Recent Progress and Future Prospects, Adv. Sci. 4 (2017) 1–21. doi:10.1002/advs.201600539.

[7] S. Yang, Y. Qiao, P. He, Y. Liu, Z. Cheng, J. Zhu, H. Zhou, A reversible lithium–CO_2 battery with Ru nanoparticles as a cathode catalyst, Energy Environ. Sci. 10 (2017) 972–

978. doi:10.1039/C6EE03770D.

[8] M. Lu, Supercapacitors: materials, systems, and applications. John Wiley & Sons, 2013.

[9] X. Wang, S. Kajiyama, H. Iinuma, E. Hosono, S. Oro, I. Moriguchi, M. Okubo, A. Yamada, Pseudocapacitance of MXene nanosheets for high-power sodium-ion hybrid capacitors., Nat. Commun. 6 (2015) 6544. doi:10.1038/ncomms7544.

[10] G. Wang, L. Zhang, J. Zhang, A review of electrode materials for electrochemical supercapacitors, Chem. Soc. Rev. 41 (2012) 797–828. doi:10.1039/C1CS15060J.

[11] M. Zhi, C. Xiang, J. Li, M. Li, N. Wu, Nanostructured carbon-metal oxide composite electrodes for supercapacitors: A review, Nanoscale. 5 (2013) 72–88. doi:10.1039/c2nr32040a.

[12] M.N. Rantho, M.J. Madito, F.O. Ochai-Ejeh, N. Manyala, an Asymmetric supercapacitor based on vanadium disulfide nanosheets as a cathode and carbonized iron cations adsorbed onto polyaniline as node, Electrochim. Acta. 260 (2017) 11–23. doi:10.1016/j.electacta.2017.11.074.

[13] H. Jiang, J. Ma, C. Li, Mesoporous carbon incorporated metal oxide nanomaterials as supercapacitor electrodes, Adv. Mater. 24 (2012) 4197–4202. doi:10.1002/adma.201104942.

[14] F. Barzegar, A. Bello, D. Momodu, M.J. Madito, J. Dangbegnon, N. Manyala, Preparation and characterization of porous carbon from expanded graphite for high energy density supercapacitor in aqueous electrolyte, J. Power Sources. 309 (2016) 245–253. doi:10.1016/j.jpowsour.2016.01.097.

[15] K.O. Oyedotun, M.J. Madito, A. Bello, D.Y. Momodu, A.A. Mirghni, N. Manyala, Investigation of graphene oxide nanogel and carbon nanorods as electrode for electrochemical supercapacitor, Electrochim. Acta. 245 (2017) 268–278. doi:10.1016/j.electacta.2017.05.150.

[16] J. Zhang, J.P. Cheng, M. Li, L. Liu, F. Liu, X.B. Zhang, Flower-like nickel-cobalt binary hydroxides with high specific capacitance: Tuning the composition and asymmetric capacitor application, J. Electroanal. Chem. 743 (2015) 38–45. doi:10.1016/j.jelechem.2015.02.021.

[17] T. M. Masikhwa, M. J. Madito, D. Y. Momodu, J. K. Dangbegnon, O. Guellati, A. Harat, M. Guerioune, F. Barzegar, N. Manyala, High performance asymmetric supercapacitor based on CoAl-LDH/GF and activated carbon from expanded graphite, RSC Adv. 6 (2016) 46723–46732. doi:10.1039/C6RA07419G.

[18] K. O. Oyedotun, M. J. Madito, D.Y. Momodu, A. A. Mirghni, T. M. Masikhwa, N. Manyala, Synthesis of ternary NiCo-MnO2nanocomposite and its application as a novel high energy supercapattery device, Chem. Eng. J. (2018) 416–433. doi:10.1016/j.cej.2017.10.169.

[19] W. Zhou, X. Cao, Z. Zeng, W. Shi, Y. Zhu, Q. Yan, H. Liu, J. Wang, H. Zhang, One-step synthesis of Ni_3S_2 nanorod@$Ni(OH)_2$ nanosheet core–shell nanostructures on a three-dimensional graphene network for high-performance supercapacitors, Energy Environ. Sci. 6 (2013) 2216–2221. doi:10.1039/C3EE40155C.

[20] H. Chen, M.R. Golder, F. Wang, R. Jasti, A.K. Swan, Raman spectroscopy of carbon nanohoops, Carbon N. Y. 67 (2014) 203–213. doi:10.1016/j.carbon.2013.09.082.

[21] W. W. Rudolph, G. Irmer, Hydration and speciation studies of Mn2+ in aqueous solution with simple monovalent anions (ClO4−, NO3−, Cl−, Br−), Dalt. Trans. 42 (2013) 14460. doi:10.1039/c3dt51493e.

[22] S. Cheng, L. Yang, D. Chen, X. Ji, Z. jie Jiang, D. Ding, M. Liu, Phase evolution of an alpha MnO2-based electrode for pseudo-capacitors probed by in operando Raman spectroscopy, Nano Energy. 9 (2014) 161–167. doi:10.1016/j.nanoen.2014.07.008.

[23] S. R. Shieh, T. S. Duffy, Raman spectroscopy of $Co(OH)_2$ at high pressures: Implications for amorphization and hydrogen repulsion, Phys. Rev. B. 66 (2002) 134301. doi:10.1103/PhysRevB.66.134301.

[24] H. D. Lutz, H. Möller, M. Schmidt, Lattice vibration spectra. Part LXXXII. Brucite-type hydroxides M(OH)2 (M = Ca, Mn, Co, Fe, Cd) — IR and Raman spectra, neutron diffraction of Fe(OH)2, J. Mol. Struct. 328 (1994) 121–132. doi:10.1016/0022-2860(94)08355-X.

[25] A. Ogata, S. Komaba, R. Baddour-Hadjean, J.-P. Pereira-Ramos, N. Kumagai, Doping effects on structure and electrode performance of K-birnessite-type manganese dioxides

for rechargeable lithium battery, Electrochim. Acta. 53 (2008) 3084–3093. doi:10.1016/j.electacta.2007.11.038.

[26] H. Xia, Y. Wang, J. Lin, L. Lu, Hydrothermal synthesis of MnO 2 /CNT nanocomposite with a CNT core/porous MnO 2 sheath hierarchy architecture for supercapacitors, Nanoscale research letters, 7(1), 33. doi:10.1186/1556-276X-7-33.

[27] K. O. Oyedotun, F. Barzegar, A.A. Mirghni, A.A. Khaleed, T. M. Masikhwa, N. Manyala, Examination of High-Porosity Activated Carbon Obtained from Dehydration of White Sugar for Electrochemical Capacitor Applications, ACS Sustain. Chem. Eng. 7 (2019) 537–546. doi:10.1021/acssuschemeng.8b04080.

[28] A. A. Khaleed, A. Bello, J. K. Dangbegnon, M. J. Madito, O. Olaniyan, F. Barzegar, K. Makgopa, K. O. Oyedotun, B. W. Mwakikunga, S. C. Ray, N. Manyala, Solvothermal synthesis of surfactant free spherical nickel hydroxide/graphene oxide composite for supercapacitor application, J. Alloys Compd. (2017) 80-91 . doi:10.1016/j.jallcom.2017.05.310.

[29] Y. Liu, R. Wang, X. Yan, Synergistic Effect between Ultra-Small Nickel Hydroxide Nanoparticles and Reduced Graphene Oxide sheets for the Application in High-Performance Asymmetric Supercapacitor, Sci. Rep. 5 (2015) 11095. doi:10.1038/srep11095.

[30] M. Naguib, T. Saito, S. Lai, M.S. Rager, T. Aytug, M. Parans Paranthaman, M.-Q. Zhao, Y. Gogotsi, $Ti_3C_2T_x$ (MXene)–polyacrylamide nanocomposite films, RSC Adv. 6 (2016) 72069–72073. doi:10.1039/C6RA10384G.

[31] W. Sun, X. Chen, Preparation and characterization of polypyrrole films for three-dimensional micro supercapacitor, J. Power Sources. 193 (2009) 924–929. doi:10.1016/j.jpowsour.2009.04.063.

[32] X. Lin, H. Li, F. Musharavati, E. Zalnezhad, S. Bae, B.-Y. Cho, O.K.S. Hui, Synthesis and characterization of cobalt hydroxide carbonate nanostructures, RSC Adv. 7 (2017) 46925–46931. doi:10.1039/C7RA09050A.

[33] F. Barzegar, A. A. Khaleed, F. U. Ugbo, K. O. Oyeniran, D. Y. Momodu, A. Bello, J. K. Dangbegnon, N. Manyala, Cycling and floating performance of symmetric supercapacitor

derived from coconut shell biomass, AIP Adv. 6 (2016) 115306 . doi:10.1063/1.4967348.

[34] X. Chen, M. Cheng, D. Chen, R. Wang, Shape-Controlled Synthesis of Co2P Nanostructures and Their Application in Supercapacitors, ACS Appl. Mater. Interfaces. 8 (2016) 3892–3900. doi:10.1021/acsami.5b10785.

[35] C. Zhao, F. Ren, X. Xue, W. Zheng, X. Wang, L. Chang, A high-performance asymmetric supercapacitor based on Co(OH)2/graphene and activated carbon electrodes, J. Electroanal. Chem. 782 (2016) 98–102. doi:10.1016/J.JELECHEM.2016.10.023.

[36] X. F. Lu, D. J. Wu, R. Z. Li, Q. Li, S. H. Ye, Y. X. Tong, G. R. Li, Hierarchical $NiCo_2O_4$ nanosheets@hollow microrod arrays for high-performance asymmetric supercapacitors, J. Mater. Chem. A. 2 (2014) 4706–4713. doi:10.1039/c3ta14930g.

[37] W. Kong, C. Lu, W. Zhang, J. Pu, Z. Wang, Homogeneous core-shell $NiCo_2S_4$nanostructures supported on nickel foam for supercapacitors, J. Mater. Chem. A. 3 (2015) 12452–12460. doi:10.1039/c5ta02432c.

[38] K. O. Oyedotun, Synthesis and characterization of carbon-based nanostructured material electrodes for designing novel hybrid supercapacitors, PhD Thesis, University of Pretoria (2018).

[39] A. Bello, F. Barzegar, M. J. Madito, D. Y. Momodu, A. A. Khaleed, T. M. Masikhwa, J. K. Dangbegnon, N. Manyala, Stability studies of polypyrole- derived carbon based symmetric supercapacitor via potentiostatic floating test, Electrochim. Acta. 213 (2016) 107–114. doi:10.1016/j.electacta.2016.06.151.

[40] A. Laheäär, P. Przygocki, Q. Abbas, F. Béguin, Appropriate methods for evaluating the efficiency and capacitive behavior of different types of supercapacitors, Elsevier B.V., 60 (2015) 21-25 . doi:10.1016/j.elecom.2015.07.022.

[41] O. Fasakin, J. K. Dangbegnon, D. Y. Momodu, M. J. Madito, K. O. Oyedotun, M. A. Eleruja, N. Manyala, Synthesis and characterization of porous carbon derived from activated banana peels with hierarchical porosity for improved electrochemical performance, Electrochim. Acta. 262 (2018) 187-196. doi:10.1016/j.electacta.2018.01.028.